Studies on bifunctional Fe(II)-triazole spin crossover nanoparticles: time-dependent luminescence, surface grafting and the effect of a silica shell and hydrostatic pressure on the magnetic properties

Journal of Materials Chemistry C

Accepted Manuscript

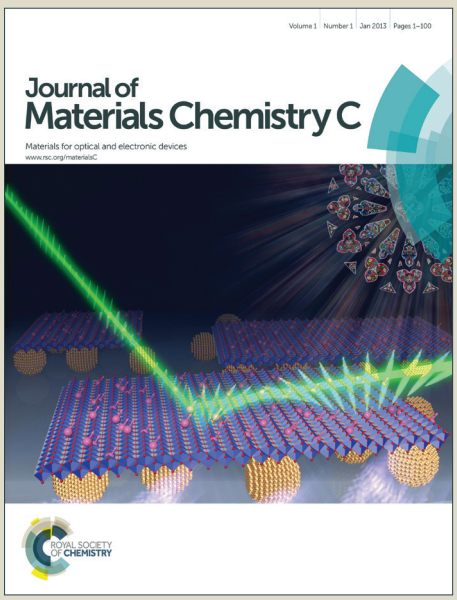

ROYAL SOCIETY OF CHEMISTRY

www.rsc.org/materialsC

Cite this: DOI: 10.1039/c0xx00000x

www.rsc.org/xxxxxx

ARTICLE TYPE

Studies on bifunctional Fe(II)-triazole spin crossover nanoparticles: time-dependent luminescence, surface grafting and effect of silica shell and hydrostatic pressure on the magnetic properties

Juan Manuel Herrera,*[a] Silvia Titos-Padilla,[a] Simon J. A. Pope,[b] Isadora Berlanga,[c] Félix Zamora,[c] Juan José Delgado,[d] Konstantin V. Kamenev,[e] Xiao Wang,[e] Alessandro Prescimone,[f] Euan K. Brechin,[f] and Enrique Colacio*[a]

Received (in XXX, XXX) Xth XXXXXXXXX 20XX, Accepted Xth XXXXXXXXX 20XX
DOI: 10.1039/b000000x

Pure and silica wrapped Fe(II)-triazole (FeHTrz) spin-crossover (SCO) nanoparticles have been prepared following a water-in-oil synthetic procedure. The size and shape can be tuned by controlling the Fe(II) and triazole concentrations in the aqueous phase. The magnetic properties of these nanoparticles are strongly affected by the presence of a silica shell embedding the nanostructured FeHTrz polymer. Whereas bare FeHTrz nanoparticles exhibit abrupt and cooperative spin transition with 24 – 35 K-wide thermal hysteresis loops, for the silica derivates the hysteresis width increases up to 37 – 42 K. This probes the efficiency of the silica shell to promote interparticle interactions and enhance cooperativity effects. Tomographic studies of the FeHTrz@SiO_2 nanoparticles reveal a core/shell structure with the pure FeHTrz polymer wrapped into a thin shell of pure silica. Taking advantage of the chemical properties of the silica shell, these hybrid nanoparticles were coated with a dansyl derivate fluorophore whose luminescent properties can be adjusted by the spin state of the SCO polymer. Time-dependent luminescent studies reveal the existence of a non-radiative energy transfer (Förster type) between the organic fluorophore and the Fe(II)-low spin ions. These nanoparticles have also been functionalized with thiol groups allowing them to be deposited onto a gold surface in a controlled manner.

1 Introduction

One of the most beautiful examples of bistability at a molecular level is the spin crossover phenomenon (SCO) observed in some coordination materials based on octahedral $3d^4$ – $3d^7$ metallic complexes.[1] In these systems, the electronic configuration of the metal can be conveniently switched from a low-spin (LS) ground state to a metastable high-spin (HS) state in response to external stimuli such as changes of temperature and/or pressure, irradiation with light (LIESST effect) or absorption/desorption processes.[2] The switching between these two spin states induces significant changes in their magnetic and optical properties, so the use of these compounds as molecular switches, thermal and/or gas sensors or as display devices has been postulated. Moreover, long-range intermolecular interactions can appear making the spin transition cooperative. Then, large thermal hysteresis loops can be observed leading to true bistability and memory effects.[3]

In order to be integrated into functional devices, SCO materials have to be prepared at the nanometer scale, whilst preserving their magnetic and cooperative behaviour. Thus, significant advances in this field have been recently achieved by different groups that focus their research activity toward the synthesis and characterization of spin-crossover nanoparticles (SCONPs).[4] Fe(II)-based coordination networks, such as the one-dimensional $[Fe(Trz)_3]X_2$ (Trz = triazole derivate; X = counter-ion) family of coordination polymers or the three-dimensional $[Fe(L)_2M(CN)_4]$ [L = pyridine derivate; M = Ni(II), Pd(II), Pt(II)] Hoffman-like systems, have been mainly used to prepare these nanoparticles since these compounds exhibit SCO behaviour with well-defined thermal hysteresis loops at temperatures close to room temperature.[5] Most of this research work has been devoted to the study of the effect of the nanoparticle size reduction on the collective behaviour responsible for the hysteresis loop, the ultimate goal being to determine the minimum size for which the nanoparticles still show thermal hysteresis. Size-controlled nanoparticles of the $[Fe(pyrazine)Pt(CN)_4]$ coordination network, prepared independently by the Real and Mallah groups, revealed a decrease of the magnetic hysteresis, abruptness of the transition and critical temperatures as the size of the nanoparticles decreased.[6] Similar results were found for nanoparticles of the $[Fe(NH_2Trz)_3]Br_2$ SCO polymer prepared by Létard et *al.*[7] Conversely, for the related system $[Fe(HTrz)_2(Trz)](BF_4)$, nanoparticles with a diameter of 11 ± 5 nm showed an abrupt spin transition above room temperature with a 40 K-wide thermal hysteresis loop. When the diameter of the nanoparticles was reduced down to 6 ± 3 nm, a 29 K-wide hysteresis was still preserved.[8] Besides size and shape, other factors such as the presence of surfactant molecules, or rigid matrices embedding the

nanoparticles, have been demonstrated to induce important modification of the magnetic behavior in these materials. For example, nanoparticles of the SCO material [Fe(pyrazine)Pt(CN)$_4$] coated with a thin shell of silica show a strongly cooperative spin transition with a 15 K-wide thermal hysteresis loop, while softer coating agents such as calixarene-based ligands, organic polymers or surfactants cancel the cooperativity.[9] Similar behaviour has also been recognized recently for 3.2(5) nm nanoparticles of the SCO polymer [Fe(Htrz)$_2$(Trz)](BF$_4$) grown within the pores of mesoporous silica monoliths, which results in a room temperature bi-stable nanocomposite with a 65 K wide hysteresis loop.[10]

In this work, we describe the synthesis of both bare and silica wrapped [Fe(Htrz)$_2$(Trz)](BF$_4$) nanoparticles following a water-in-oil synthetic procedure. The size and shape of the nanoparticles can be precisely tuned by controlling the Fe(II) and HTrz concentrations. Both types of nanoparticle show a strongly cooperative spin transition, although wider hysteresis loops are observed for the hybrid Fe(II)/SiO$_2$ nanoparticles. These results confirm the important role of the surrounding silica matrix in favouring the propagation of long range elastic interactions that enhance cooperativity.

We have reported previously the use of silica to wrap nanoparticles of the SCO system [Fe$_{0.5}$Zn$_{0.5}$(HTrz)$_2$(Trz)](BF$_4$) to which a dansyl derivate luminophore (3-(dansylamido)propyltrimethoxysilane) was attached leading to bifunctional SCO/luminescent materials. In these hybrid systems, the dansyl emission intensity appeared to be synchronized with the LS ↔ HS transition[11], so that the dansyl emission is quenched by the Fe(II) low spin ions in the core of the nanoparticles since there exists a spectral overlap between the dansyl luminescence and the LS absorption band $^1A_1 \rightarrow {}^1T_1$ of the Fe(II) ions. This was one of the several examples reported in the last few years in which bifunctional nanoparticles combining SCO and luminescence properties have been prepared.[12] The modulation of a luminescent signal through a LS ↔ HS transition is a very interesting phenomenon that could find applications in several fields, such as thermometry, sensors, biomarkers or photonic switches. The SCO phenomenon could be registered easily through changes in the luminescent signal rather than using other techniques such as magnetometry. Bousseksou and co-workers prepared nanoparticles of the SCO [Fe(NH$_2$Trz)$_3$](OTs)$_2$ (NH$_2$Trz = 4-amino-1,2,4-triazole; OTs = tosyl) doped with the fluorescent agent Rhodamine 110. The emission spectrum to the fluorophore overlaps with the $^1A_1 \rightarrow {}^1T_1$ absorption band of the Fe(II) polymer in the LS state and the emission is partially quenched. The authors suggested that this behaviour was due to a radiative (trivial) energy transfer mechanism between the Rhodamine and the Fe(II)-LS core.[13] By replacing the Rh-110 fluorophore by acridine orange, a better spectral overlap between the emission spectrum and the $^1A_1 \rightarrow {}^1T_1$ absorption band of the Fe(II)-LS complex exists, leading to an increase in the efficiency of the energy transfer, which in this case was largely attributed to a non-radiative mechanism (FRET).[14] However, no experimental probes regarding the nature of the energy transfer process were presented. Indeed, the uncertainty of the fluorophore location in the nanoparticle introduces significant difficulties in understanding the mechanism governing the energy transfer process in these hybrid materials. We pursue this study further and time-dependent luminescence studies demonstrate that, in our systems, the quenching of the dansyl emission in the LS regime is due to a non-radiative energy transfer process (Förster type). We have also functionalized the surface of hybrid Fe(II)/SiO$_2$ nanoparticles with thiol groups which allows them to be homogeneously deposited onto a gold surface.

2 Experimental

2.1 Materials and chemicals

All chemicals used were obtained from commercial sources and used without further purification. Bulk [Fe(Htrz)$_2$(Trz)](BF$_4$) was prepared as reported previously.[15] Gold surfaces for Atomic Force Microscopy (AFM) studies were commercially purchased from the Arrandee Company.

2.2 Instrumentation and characterization

Nanoparticles were characterized by Transmission electron microscopy (TEM) using a Philips CM-20 HR electron microscope operating at 200 keV. 5 mg of the material was redispersed by sonication (30 min) in 1 mL of EtOH. Carbon reinforced copper grids (200 meshs) were submerged into de suspension 50 times and then allowed to dry on air for at least 48 h. The size of the particles was determined by "manual counting" using ScionImage software (http://www.scioncorp.com). HAADF-STEM images were recorded on a JEOL2010 FEG instrument working at an accelerating voltage 200 KV in scanning mode with a probe diameter of 0.5 nm. Elemental analyses were carried out at the "Centro de Instrumentación Científica" (University of Granada) on a Fisons-Carlo Erba analyser model EA 1108. Magnetic measurements were obtained with the use of a Quantum Design SQUID magnetometer MPMS-XL operating at a magnetic field of 10000 G in the 310 – 400 K range of temperature. The heating-cooling cycles were done with a rate of 10 Kmin^{-1}. A long gas-driven pressure cell similar to the piston-cylinder pressure cell with helium gas as pressure-transmitting medium,[16] was used for measuring magnetic susceptibility at high-pressure. Photoluminescence spectra were measured by a Varian Cary Eclipse spectrofluorometer on solid samples by using a home-built setup that collected the emitted signal in the range 400-280 K. Lifetime data were obtained on a JobinYvon-Horiba Fluorolog spectrometer fitted with a JY TBX picoseconds photodetection module. The pulsed source was a Nano-LED configured for 295 nm output operating at 1 MHZ. The detector response was obtained using Ludox SiO$_2$ as a scatterer. Luminescence lifetime profiles were obtained using the JobinYvon-Horiba FluoroHub single photon counting module and the data fits yielded the lifetime values using the provided DAS6 deconvolution software. Atomic Force Microscopy (AFM) images were acquired in dynamic mode using a Nanotec Electronica system (www.nanotec.es). Olympus cantilevers were used with a nominal force constant of 0.75 N/m.

2.1 Synthesis of [Fe(Htrz)$_2$(Trz)](BF$_4$) nanoparticles (FeHTrz NPs)

1. An aqueous solution of Fe(BF$_4$)$_2$·6H$_2$O (337 mg, 1 mmol in 0.5 mL of deionized H$_2$O) was added to a solution containing Triton X-100 (1.8 mL), *n*-hexanol (1.8 mL) and cyclohexane (7.5 mL).

The resulting mixture was stirred until formation of a clear water-in-oil microemulsion. A similar procedure was applied to 1,2,4-*1H*-Triazole (Htrz) (210 mg, 3 mmol in 0.5 mL of deionized H_2O). Both microemulsions were quickly combined and the mixture stirred for 24 h into the dark, followed by addition of acetone to break the microemulsion. The precipitated nanoparticles were recovered by centrifugation washed several times with EtOH, then acetone and finally dried at 70 ºC for 12 h. In this case, the iron(II) concentration in water, $c(Fe^{II})$, was 1 M.

2. The material was prepared following the same synthetic procedure as in sample **1**, but using 0.75 mmol of $Fe(BF_4)_2{\cdot}6H_2O$ (253 mg) and 2.25 mmol of Htrz (158 mg). In this case, $c(Fe^{II})$ = 0.75 M.

3. The material was prepared following the same synthetic procedure as in sample **1**, but using 0.625 mmol of $Fe(BF_4)_2{\cdot}6H_2O$ (211 mg) and 1.875 mmol of Htrz (131 mg). In this case, $c(Fe^{II})$ = 0.625 M.

4. The material was prepared following the same synthetic procedure as in sample **1**, but using 0.5 mmol of $Fe(BF_4)_2{\cdot}6H_2O$ (169 mg) and 1.5 mmol of Htrz (105 mg). In this case, $c(Fe^{II})$ = 0.5 M.

2.2 Synthesis of hybrid {[Fe(Htrz)$_2$(Trz)](BF$_4$)}@SiO$_2$ nanoparticles (FeHTrz@SiO$_2$NPs)

1@SiO$_2$. An aqueous solution of $Fe(BF_4)_2{\cdot}6H_2O$ (337 mg, 1 mmol in 0.5 mL of deionized H_2O) and 0,1 mL of TEOS were added to a solution containing Triton X-100 (1.8 mL), *n*-hexanol (1.8 mL) and cyclohexane (7.5 mL). The resulting mixture was stirred until formation of a clear water-in-oil microemulsion. A similar procedure was applied to 1,2,4-*1H*-Triazole (Htrz) (210 mg, 3 mmol in 0.5 mL of deionized H_2O). Both microemulsions were quickly combined and the mixture stirred for 24 h into the dark, followed by addition of acetone to break the microemulsion. The precipitated nanoparticles were recovered by centrifugation, washed several times with EtOH, then acetone and finally dried at 70 ºC for 12 h. In this case, the iron(II) concentration in water, $c(Fe^{II})$, was 1 M.

2@SiO$_2$. The material was prepared following the same synthetic procedure as in sample **1@SiO$_2$**, but using 0.75 mmol of $Fe(BF_4)_2{\cdot}6H_2O$ (253 mg) and 2.25 mmol of Htrz (158 mg). In this case, $c(Fe^{II})$ = 0.75 M.

3@SiO$_2$. The material was prepared following the same synthetic procedure as in sample **1@SiO$_2$**, but using 0.625 mmol of $Fe(BF_4)_2{\cdot}6H_2O$ (211 mg) and 1.875 mmol of Htrz (131 mg). In this case, $c(Fe^{II})$ = 0.625 M.

4@SiO$_2$. The material was prepared following the same synthetic procedure as in sample **1@SiO$_2$**, but using 0.5 mmol of $Fe(BF_4)_2{\cdot}6H_2O$ (169 mg) and 1.5 mmol of Htrz (105 mg). In this case, $c(Fe^{II})$ = 0.5 M.

2.3 Surface functionalization of 1@SiO$_2$ with dansyl-derivate fluorophores, 1@SiO$_2$-Dansyl

Decoration of the surface of **1@SiO$_2$** with dansyl groups was achieved following the procedure previously reported by us.[11] Thus, 0.1 g of 1@SiO_2 and 0.025 g (0.055 mmol) of 3-(dansylamido)propyltrimethoxysilane were added to a mixture of dried acetonitrile/dichloromethane (1:1, 50 mL). The resulting mixture was heated at reflux for 48 h in an inert atmosphere. The solid nanoparticles were recovered by centrifugation and washed several times with acetonitrile, ethanol and acetone until the dansyl fluorescence had vanished in the solvent. The final solid was dried at 70 ºC for 12 h.

2.4 Surface functionalization of 1@SiO$_2$ with thiol groups, 1@SiO$_2$-SH

200 µL (1 mmol) of 3-mercaptopropyltrimethoxysilane (MPTMS) were added to a suspension of 0.1 g of **1@SiO$_2$** in 40 mL of dry acetonitrile. The mixture was stirred at reflux for 48 h in an inert atmosphere. The solid nanoparticles were recovered by centrifugation and washed several times with acetonitrile, ethanol and acetone to remove any MPTMS molecules non grafted to the 1@SiO_2 surface. Finally, the solid was dried at 70 ºC for 12 h.

2.5 Sample preparation of 1@SiO$_2$-SH for AFM measurements

Cleaning of the Gold Surfaces. In order to obtain reproducible results, gold substrates were treated just before the chemical deposition. They were immersed on a solution of H_2SO_4:H_2O_2 (2:1) for 10 min., then washed with water, sonicated 5 min. (680 w, 20 ºC) on water, and exposed to direct flame for 2 min.

Dispersion Procedure of 1@SiO$_2$-SH nanoparticles. 1 mg of 1@SiO_2-SH nanoparticles in 1 mL of ethanol was sonicated with an ultrasonication bath (Elma, 37 kHz, 380 W) for 30 min.

Adsorption of 1@SiO$_2$-SH on Gold surface. Gold surfaces were immersed in the 1@SiO_2-SH ethanol suspension (1 mg/mL) for 6-12 h, washed with ethanol and then dried with an argon flow.

3 Results and discussion

3.1 Synthesis and structural characterization

Nanoparticles of the SCO polymer $\{[Fe(Htrz)_2(Trz)](BF_4)\}_n$ **1 – 4** were prepared following a classical reverse micelle approach. The syntheses were performed at room temperature by mixing two separate microemulsions, both containing adequate amounts of a surfactant (Triton X-100), a co-surfactant (*n*-hexanol), and a hydrocarbon (cyclohexane) as organic phase. One of the microemulsions contained an aqueous solution of the iron salt whereas the other one contained the stoichiometric amount of HTrz ligand, dissolved in the same amount of water. A few minutes after the microemulsions were mixed and vigorously stirred, the color of the mixture turned purple confirming the formation of the coordination polymer $\{[Fe(HTrz)_2(Trz)](BF_4)\}_n$ *via* content exchange between the microdroplets of both microemulsions. The stirring was maintained for 24 h and then acetone was added to break down the emulsion leading to the precipitation of the Fe-Trz nanoparticles which were successfully recovered by centrifugation after several washing cycles. For the synthesis of the nanoparticles, all the synthetic parameters were kept constant except the Fe(II) and HTrz concentrations in water. Thus, syntheses at $C_{[Fe(II)\ in\ water]}$ = 1 , 0.75 , 0.625 and 0.5 M, respectively, yielded **1**, **2**, **3** and **4** as purple solids at room temperature.

HR-TEM and HR-SEM images for samples **1 - 4** are shown in Figure 1. In all cases, the nanoparticles are monodisperse, homogeneous and well defined. **1** is made of quasi-spherical nanoparticles with a mean diameter of 28.3 ± 2.9 nm. Nanoparticles of **2** show a roughly cubic-like topology with a side length of 38.4 ± 2.6 nm. Compound **3** shows a slightly

rectangular shape with an average length of 70.3 ± 6.5 nm and a width of 59.0 ± 4.3 nm. Complex **4** consists of rod-like nanoparticles with a side length of 321.2 ± 17.1 nm and a width of 194.9 ± 16.3 nm. These images show how as the $C_{Fe(II)}$ decreases, the Fe-Trz nanoparticles increase significantly their size. The higher the concentration of the precursors, the smaller the size of the nanoparticles. This fact is in agreement with that expected for a nucleation-controlled process, where a higher concentration of precursors induces the formation of a larger amount of nuclei, thus leading to smaller particles. A similar size dependence on the concentration of the precursors has been previously observed for other SCONPs.[17] Moreover, as the size of the nanoparticle increases, they tend to adopt a rod-like topology similar to that shown by the particles of the bulk material prepared in a classical manner (Figure S1 in ESI).

Hybrid FeHTrz@SiO_2 nanoparticles were prepared following the same synthetic approach as for samples **1 – 4**, but adding an hydrophilic precursor of silica, tetraethyl orthosilicate (TEOS), to the Fe(II) and HTrz microemulsions. Thus, in these cases, the FeHTrz NPs are embedded within a silica shell formed by the sluggish hydrolysis and polymerization of TEOS. As before, all the synthetic parameters were kept constant except the Fe(II) and HTrz concentrations in water. Thus, syntheses at $C_{[Fe(II)\ in\ water]}$ = 1 , 0.75 , 0.625 and 0.5 M, respectively, yielded **1@SiO_2**, **2@SiO_2**, **3@SiO_2** and **4@SiO_2** as purple solids at room temperature.

As observed for **1 - 4**, the nanoparticles tend to both adopt a rod-like morphology and increase their dimensions as the reactants Fe(II) and HTrz concentration decreases (Figure 2). However, in this case the mean size of the nanoparticles **1 - 4@SiO_2** is significantly higher compared to the analogues **1 – 4** prepared in absence of TEOS (Table 1). In order to fully characterize the composition, the structure and the distribution of silica and the Fe(II) polymer in these kind of nanoparticles, high-angle annular dark-field scanning transmission electron microscopy (HAADF-STEM) tomography studies were performed on sample **3@SiO_2**. The tomographic reconstruction was achieved by tilting the specimen on one axis with respect to the electron beam and collecting a series of two-dimensional HAADF-STEM images at a range of tilts. Figure 3a shows a HAADF-STEM image acquired through the tomographic acquisition. Considering the atomic numbers of iron (Z_{Fe} = 26) and silicon (Z_{Si} = 14), which are the main elements forming the Fe(II) polymer and the silica matrix respectively, it is clear that nanocomposite **3@SiO_2** is made of an iron rich core (brighter) with dimensions of *ca.* 100 × 50 nm and surrounded by a thin shell (~ 12 nm in width) of pure silica. A surface-rendered tomographic reconstruction is shown in Figure 3b. These results confirms that nanoparticles **1 – 4@SiO_2NPs** are of the core-shell type with the Fe(II) polymer located at the core of the nanoparticles and surrounded by a narrow shell of pure silica.

3.2 Magnetic properties

Figure 4 shows the thermal dependence of $\chi_M T$ for **1 – 4** and **1 – 4@SiO_2** (χ_M is the magnetic susceptibility and T is the temperature). For **1 – 4**, the $\chi_M T$ values at 400 K range between 3.53 – 3.62 $cm^3 \cdot K \cdot mol^{-1}$, which fit well with the expected value for an Fe(II) ion with high-spin electronic configuration . In all the cases, the $\chi_M T$ values at 310 K reveal the existence of a residual HS population at low temperature. This HS fraction is attributed to Fe atoms located at the surface of the nanoparticle which are partially coordinated by water molecules [$Fe(Trz)_{3-x}(H_2O)_{2x}$ with $0 < x > 3$] and therefore remain at the HS state in all the temperature range. This fraction is much higher than that found in the bulk (10 %) and generally increases as the size of the nanoparticle decreases (Table 2). This increase is attributed to surface effects on the nanoparticles. Thus, as the nanoparticles are larger, their proportional surface area decreases and, consequently, the fraction of partially coordinated Fe(II) ions. In all cases the spin transition is abrupt and shows a well-shaped thermal hysteresis loop with critical temperatures located above room-temperature. In general, the hysteresis width is close to 25 K except for sample **4**, in which this width slightly rises up to 35 K. In this last case, the hysteresis width is quite close to that shown by the bulk. Thus a correlation between the thermal hysteresis width and the size of the nanoparticle can be established: when the size of the nanoparticle is large, *i.e.* 321.2 nm for **4**, the values of the critical temperatures are similar to those of the bulk (microparticles), whereas for nanoparticles with size in the 70 - 28 nm range, the hysteresis width slightly decreases, although the spin transition is always abrupt and with hysteresis. This trend is similar to that observed by Létard[7] in nanoparticles of the polymer $[Fe(NH_2\text{-}Trz)_3]Br_2 \cdot 3H_2O$ (NH_2-Trz = 2-amino-1,2,4-triazole) where the magnetic properties of nanoparticles larger than 200 nm were very similar to those observed for the bulk. For particles of sizes between 160 – 80 nm, the spin transition becomes more gradual with the hysteresis width being less pronounced. However, in this example, the hysteresis vanishes completely when the particle size is reduced to 50 nm, whereas in our case, a ~ 25 K wide hysteresis loop is still observed.

Most of the previous comments apply also for **1 – 4@SiO_2** although two important differences are observed. Firstly, the percentage of remnant HS population at low temperature is significantly higher in these cases, up to an additional 3.9 % in the case of **4@SiO_2** compared to **4**. Secondly, the thermal hysteresis loops for these samples are significantly wider, being in all cases close to 40 K and very similar to that shown by the bulk sample, being almost independent of the particle size. Thus it appears evident that the cooperativity of the spin transition in these systems increases when they are enveloped within a silica shell to reach a maximum close to 40 K in width which is independent of the size of the particle. This behaviour confirms the ability of the silica shell of the nanoparticle to transmit the elastic vibrations generated from the LS - HS switch to other nanoparticles located in the vicinity, increasing the efficiency of the inter-particles interactions and thus the cooperativity. Nevertheless, the effect of the coating on the width of the thermal hysteresis is a complex phenomenon and other factors such as chemical pressure, viscosity, chemical interactions between core and shell can also play a significant role.[18]

In order to examine the effect of pressure on the SCO properties of the nanoparticles **1**-**4** and **1**-**4@SiO_2** we have measured, as an example, the temperature dependence of $\chi_M T$ of the nanoparticles prepared with a 1 M iron(II) concentration (**4** and **4@SiO_2**) under hydrostatic pressures of 0.004, 0.008. 0.012 and 0.016 GPa.

Both materials exhibit a slight pressure dependence of the

temperature dependence of $\chi_M T$ in the pressure range studied, their $T_c\uparrow$ and $T_c\downarrow$ being shifted to higher temperatures as the hydrostatic pressure increases. This behaviour is mainly due to the increase in the inter-particle interaction with increasing pressure, leading to shorter Fe-N distances and larger crystal field that favours the LS state. In fact, at 0.01 GPa the paramagnetic HS state is suppressed in both materials. The temperature dependences of $T_c\uparrow$ and $T_c\downarrow$ are not identical, the latter being larger than the former. It is worth mentioning that the hysteresis width is almost independent of the applied pressure in the 0.004-0.016 GPa range. Nevertheless, the hysteresis for **4@SiO$_2$** is higher than that for **4** (47. 0 K and 55.4 K, respectively), which agrees, as indicated above, with the effectiveness of the silica shell to transmit inter-particle interactions. SCO systems generally follow a linear dependence of T_c with pressure,[19] which using the mean field theory of phase transitions in spin cross-over compounds is expressed by the Clasius-Clapeyron equation:[20]

$$T_c(p) = T_c + p(\Delta V/\Delta S) \quad (1)$$

in which $\Delta V/\Delta S = \partial T_c(p)/\partial p$ represents the average pressure dependence of $T_c(p)$ and ΔV and ΔS are the change of volume and entropy per mol of compound upon the SCO transition. The linear fitting of the pressure dependence of $T_{1/2}$ (average of $dT_{1/2}\downarrow/dp$ and $dT_{1/2}\uparrow/dp$) to the above equation leads to slopes of 290(66) KGpa^{-1} (R^2 = 0.91) and 230(21) KGpa^{-1} (R^2 = 0.98) for **4** and **4@SiO$_2$**, respectively, which demonstrate their large pressure efficiency on the transition temperature (Figure 6).

The extracted values are close to those observed for related 1D coordination polymers containing triazole derivatives bridges, such as [Fe(hyptrz)]$_3$(4-chorophenylsulphonate)·H$_2$O and [Fe(hyptrz)]$_3$(4-chorophenylsulphonate)[21] with $dT_{1/2}/dp$ values of 240 and 230 KGpa^{-1}, but higher than those for mononuclear complexes, such as [Fe(dpa)$_2$(NCS)$_2$] (dpa = 2,2-dipyridylamine),[22] [Fe(abpt)$_2$(NCS)$_2$] (abpt = 4-amino-3,5-bis(pyridine-2-yl)-1,2,4-triazol)[23] and [Fe(2-pic)$_3$(NCS)$_2$] (2-pic = 2-aminomethylpyridine)[24] with dT$_{1/2}$/dp values 187.5, 176 and 150 K, respectively.

3.3 Surface decoration of 1@SiO$_2$ with dansyl-fluorophore derivates

As commented above, we have demonstrated that Fe/Zn-Trz@SiO$_2$ nanoparticles are an excellent platform to prepare bifunctional SCO-Luminescent materials by grafting alkoxysilane-derivate organic fluorophores to the surface of the nanoparticles. Thus, hybrid Fe/Zn-Trz@SiO$_2$-danysl nanoparticles (with dansyl being 5-dimethylamino-1-naphthalenesulfonamido chromophoric groups) were prepared and it was found that changes in the fluorescence intensity of the dansyl groups were synchronized with the thermally induced SCO transition. At 280 K, LS regime, after irradiation at 315 nm a broad fluorescence band with λ_{max} = 495 nm typical of dansyl groups was observed. When the temperature rose up to 400 K (HS regime), conversely to the expected thermal quenching of the fluorescence, the emission intensity increased significantly. This odd behaviour was explained by considering the existence of a donor/acceptor energy transfer process from the dansyl groups to the Fe(II)-LS complex since a reasonable spectral overlap exists between the dansyl fluorescence band and the LS absorption band $^1A_1 \rightarrow {}^1T_1$ of the Fe(II) ion. The thermal variation of the emission intensity monitored at 495 nm of [Fe$_{0.5}$Zn$_{0.5}$(HTrz)$_2$(Trz)](BF$_4$)@SiO$_2$ nanoparticles closely followed the SCO curve obtained from magnetic studies. To confirm if undiluted [Fe(HTrz)$_2$(Trz)](BF$_4$)@SiO$_2$ nanoparticles showed a similar behaviour, the thermal variation of the magnetic and luminescent properties of **1-@SiO$_2$-dansyl** were studied. Compared to **1**, the SCO transition of **1-@SiO$_2$-dansyl** displays a slightly wider thermal hysteresis loop ($T_c\uparrow$ = 382 K, $T_c\downarrow$ = 332 K, ΔT = 50 K) which is probably due to the higher degree of agglomeration observed for these nanoparticles (Figures S2-S3, ESI). Room-temperature irradiation of **1-@SiO$_2$-dansyl** at λ_{exc} = 315 nm, led to the appearance of a broad emission band centered at *ca*. 495 nm, typical of dansyl groups. When the temperature rose up to 400 K, the 4-fold increase of the emission intensity was observed. To confirm if, as observed for the diluted Fe$_{0.5}$/Zn$_{0.5}$ nanoparticles, the increase of the intensity was synchronized with the SCO transition, two cycles of the thermal variation of the fluorescence intensity at λ_{em} = 494 nm were measured (Figure 7). This variation described a thermal hysteresis loop which was quite similar to that observed for the thermal variation of χ_MT. For both cycles, the critical cooling and heating temperatures (cycle 1: $T_c\uparrow$ = 393 K, $T_c\downarrow$ = 336 K, ΔT = 57 K; cycle 2: $T_c\uparrow$ = 391 K, $T_c\downarrow$ = 338 K, ΔT = 53 K) are similar to that reported from magnetic measurements. Nevertheless, above 395 K an anomalous behaviour is observed for the emission intensity. In this study, the sample was first heated until 410 K and then the emission intensity at λ_{em} = 495 nm was recorded as the temperature decreased at a rate of 10 Kmin^{-1}. Between 410 and 395 K, the emission is slightly attenuated as the temperature decreases. Below 395 K, the intensity remains almost constant until $T_c\downarrow$ = 336 K, when the emission intensity falls dramatically coinciding with the Fe^{II}(HS) → Fe^{II}(LS) transition. Below 330 K, the emission reached a minimum that remained constant until the cooling cycle finished at 315 K. Then, the temperature was raised at 10 Kmin^{-1} with no significant variance of the emission intensity until 390 K after which, the emission intensity increased sharply coinciding now with the Fe^{II}(LS) → Fe^{II}(HS) transition. Above 395 K, the emission intensity started to decrease again which prevented the hysteresis loop from being closed. For the second thermal cycle the same behaviour is observed although the emission in the HS and LS regimes was 20.5 % less intense. The decrease of intensity observed between both cycles is probably due to the fact that the danysl groups grafted to the surface of the nanoparticles decompose thermally when the temperature rises above 395 K. To confirm this hypothesis, a fresh sample was subdued to successive heating (400 K) – cooling (300 K) cycles and a gradual and irreversible decrease of the emission intensity was observed which confirmed the thermal decomposition of the dansyl groups at temperatures close to 400 K. As stated above, in the last few years, several examples of bifunctional SCO/luminescent nanoparticles in which the spin transition tuned the emission intensity were reported. However, the energy transfer mechanism regulating this behavior remains unclear. In these hybrid nanomaterials, the uncertainty in the precise location of the donor (fluorophore)/acceptor (Fe^{II}(LS)) pairs renders great difficulty in the determination of the energy-transfer mechanism. Two different quenching mechanisms have

been most commonly proposed: *i)* a radiative energy transfer process (inner filter effect) and *ii)* a Förster-type non-radiative energy transfer process (FRET). Both mechanisms require an overlap between the donor emission and the acceptor absorption spectra. For a radiative energy transfer, the donor absorbs energy and then emits a photon which is reabsorbed by the acceptor leading to a quenching of the donor emission. However, both entities are independent of each other so the emission lifetime of the donor is not affected by the presence of the acceptor. Conversely, a non-radiative energy transfer constitutes an additional pathway to deactivate the donor's excited state and the emission lifetime is reduced.[25] Thus, to determine the mechanism of the energy transfer process, it is necessary to determine how the emission lifetime of the dansyl groups are affected by the presence of the energy acceptors Fe^{II}(LS) centres. As the excited state lifetime of the dansyl groups are sensitive to the surrounding polarity and/or rigidity,[26] pure amorphous Ludox AS-40 SiO_2 nanoparticles were prepared and their surface functionalized with dansyl groups following the same synthetic approach used to prepare **1-@SiO$_2$-dansyl**. In these nanoparticles, the environment of the dansyl moieties is similar to that found in the Fe-Trz@SiO_2 nanoparticles but the Fe^{II}(LS) quenchers are absent. Room-temperature time-resolved luminescent experiments performed on these nanoparticles allowed to determine an excited state lifetime of 12.0 ns. For **1-@SiO$_2$-dansyl**, the lifetime measured under the same conditions (LS regime) was found to be significantly lower, 7.4 ns. This result strongly supports the existence of a dansyl→Fe^{II}(LS) non-radiative energy transfer with a rate K_{EnT}, of ca. $5.3 \cdot 10^7$ s^{-1} (on the basis of equation 5 where τ_q is the "quenched" dansyl lifetime in the presence of Fe^{II}(LS) centres and τ_u is the "unquenched" lifetime in this particular environment). The efficiency of the energy transfer can be estimated to be 38.8% by equation 7.

$$K_{EnT} = 1/\tau_q - \tau_u \quad (5)$$

$$K_{in} = 1/\tau_u \quad (6)$$

$$\eta_{EnT} = K_{EnT} \cdot (K_{EnT} + K_{in})^{-1} \quad (7)$$

Thus, the decrease of both, the dansyl excited-state emission intensity and lifetime in the LS regime suggests the existence of a Förster-type energy transfer from these groups localized at the outer shell of the nanoparticle to the Fe^{II}-(LS) moiety located at the core. This synergy has been previously observed by us in hybrid core/shel silica nanoparticles[27] and demonstrates that SiO_2 nanoparticles are an excellent platform to prepare multimodal nanomaterials exhibiting synergy between core- and shell-active components.

3.4 Surface decoration of 1@SiO$_2$ with thiol groups and deposition onto a gold surface. Atomic Force Microscopy Characterisation

The surface of silica nanoparticles can also be decorated with functional groups such as thiol, amino or carboxylic acid and then grafted onto substrates such as gold or silicon films through covalent bonds. To explore this possibility, sample **1@SiO$_2$** has been functionalized with MPTMS and then deposited onto a gold surface. A clean gold surface was dip-coated into a suspension of **1@SiO$_2$-SH** in ethanol for 12 h, washed with ethanol and dried under an Argon flow. The covered gold surface was imaged by AFM. As shown in Figure 8, the gold surface shows a high density of nanoparticles homogeneously distributed with few aggregates. The mean particle height, 52.2 ± 4.8 nm, is in good agreement with the size determined by TEM, and indicates that the gold surface is covered by a single monolayer of nanoparticles.

The attachment of **1@SiO$_2$-SH** to the gold surface can be controlled by the immersion-time of the surface into the ethanol suspension of **1@SiO$_2$-SH**. Thus a statistical analysis of the number of particles attached to the surface at different immersion times shows that at after 12 h of immersion the coverage is *ca*. 19 ± 1 particles/μm^2, while shorter immersion times led to a less homogenous distribution and a density of *ca*. 13 ± 1 particles/μm^2. Shorter immersion times (1-3 h) show a significant reduction of particles attached to the surface, in fact we cannot properly estimate the density of particles because single particles were just eventually detected on the surfaces (Figure S4).

Conclusions

In conclusion, Fe(II)-triazole SCO nanoparticles have been prepared by a reverse micelle synthetic approach. We demonstrate how the Fe(II) and HTrz concentrations in the aqueous phase exert a fine control of the size and shape of the formed nanoparticles. For the materials with particle's size in the 28 – 70 nm range, the spin transition shows 25 K-wide thermal hysteresis loops, whereas for larger nanoparticles the hysteresis width increases up to 35 K. Adding a silica precursor to the microemulsion allows to obtain core/shell nanoparticles in which the FeTrz polymer is embedded within a thin shell of silica. The cooperativity of the spin transition in these core/shell nanoparticles is significantly enhanced and the thermal hysteresis width increases up to 40 K independently of the size of the nanoparticles, which demonstrate the ability of the rigid silica shell to promote interparticles interactions.

The magnetic properties of **4** and **4**@SiO_2, in the form of $\chi_M T$ *vs* T, show slight pressure dependence, which results in an increase of both $T_c\uparrow$ and $T_c\downarrow$ when the hydrostatic pressure is augmented in the 0.004-0.016 GPa range. This behavior is due to the increase of the interparticle interactions as the pressure is raised. At 0.01 GPa the Fe-N distances are shortened in such an extent that the crystal field around Fe^{II} atom is enough to suppress the paramagnetic HS state in both complexes. The pressure dependence of $T_{1/2}$ follows the Clausius-Clapeyron equation with high $dT_{1/2}/dp$ values, thus demonstrating the large pressure efficiency on the transition temperature for these materials.

Additionally the silica shell in these nanoparticles allowed us to attach to their surface a dansyl derivate fluorophore leading to a bifunctional SCO-luminescent material in which the spin configuration of the FeTrz core controls the emission intensity of the fluorophore. Time-resolved luminescence studies demonstrate that in the LS state, the dansyl emission is partially quenched through a dansyl→Fe(II) non-radiative energy transfer process (Förster type). Similarly, thiol groups can be grafted to the surface of these nanoparticles which allow them to be attached to gold surfaces in a controlled manner by dip-coating. AFM analysis allows to determine the shape and dimension of the

nanoparticles. The control of immersion time of the gold surface in ethanol suspensions of the thiol-functionallized nanoparticles allows to modulate the density of particles anchored to the surface. This is an important aspect regarding potential devices fabrication.

Cite this: DOI: 10.1039/c0xx00000x

www.rsc.org/xxxxxx

ARTICLE TYPE

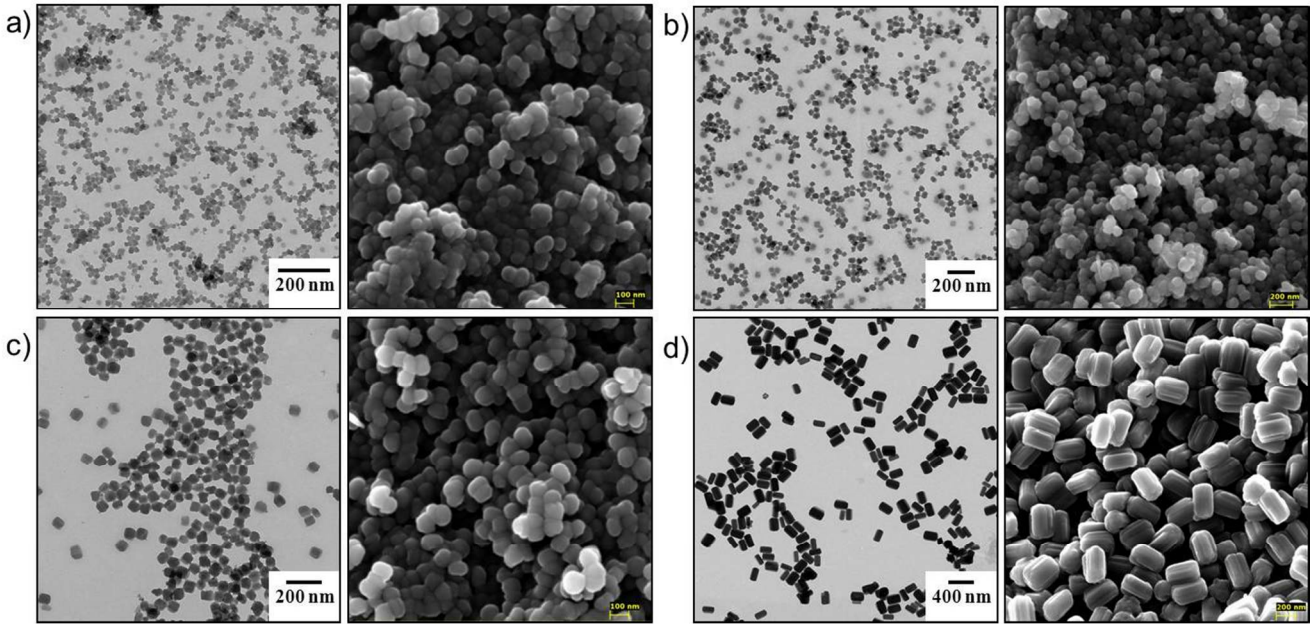

Fig. 1 HR-TEM (left) and HR-SEM (right) images for samples **1** (a), **2** (b), **3** (c) and **4** (d).

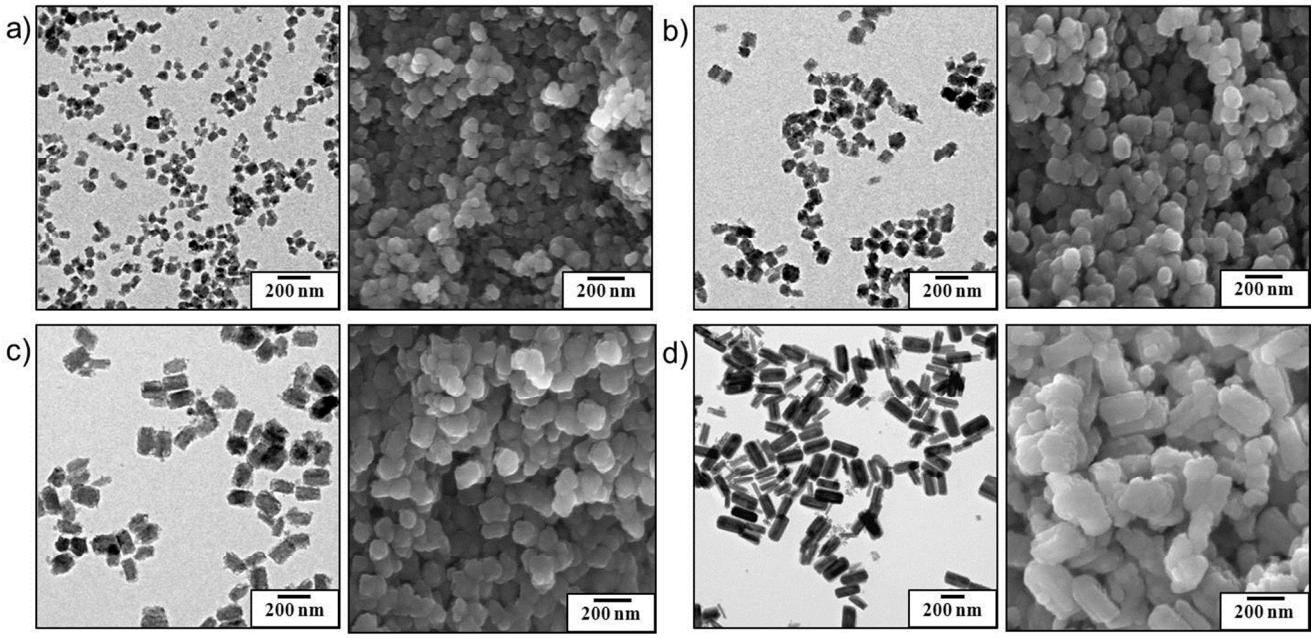

Fig. 2 HR-TEM (left) and HR-SEM (right) images for samples **1@SiO$_2$** (a), **2@SiO$_2$** (b), **3@SiO$_2$** (c) and **4@SiO$_2$** (d).

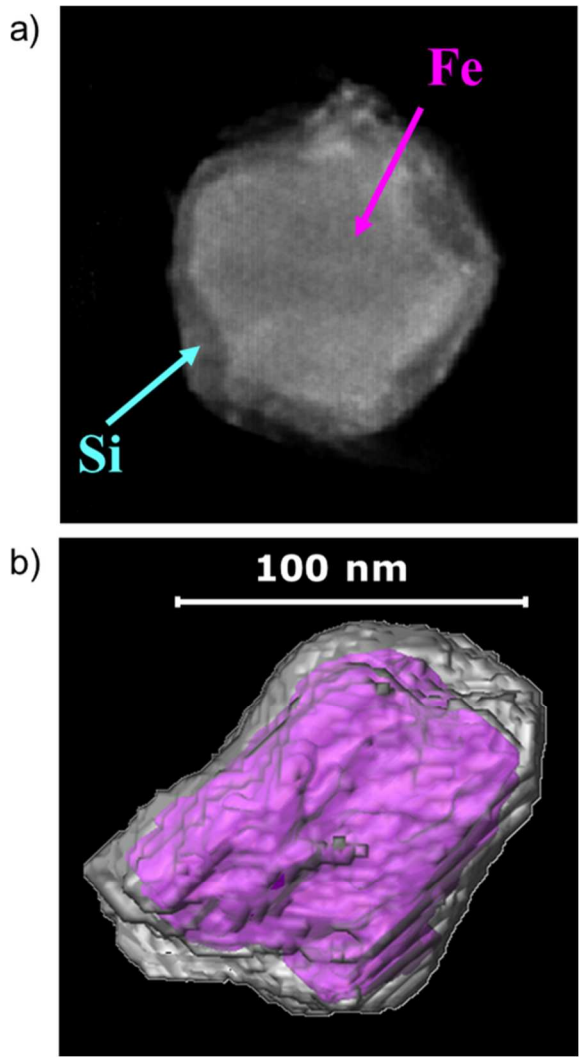

Fig. 3 a) A two-dimensional HAADF-STEM image collected through the tomographic acquisition showing the core/shell structure of the nanoparticle. b) A three-dimensional surface rendered tomographic reconstruction.

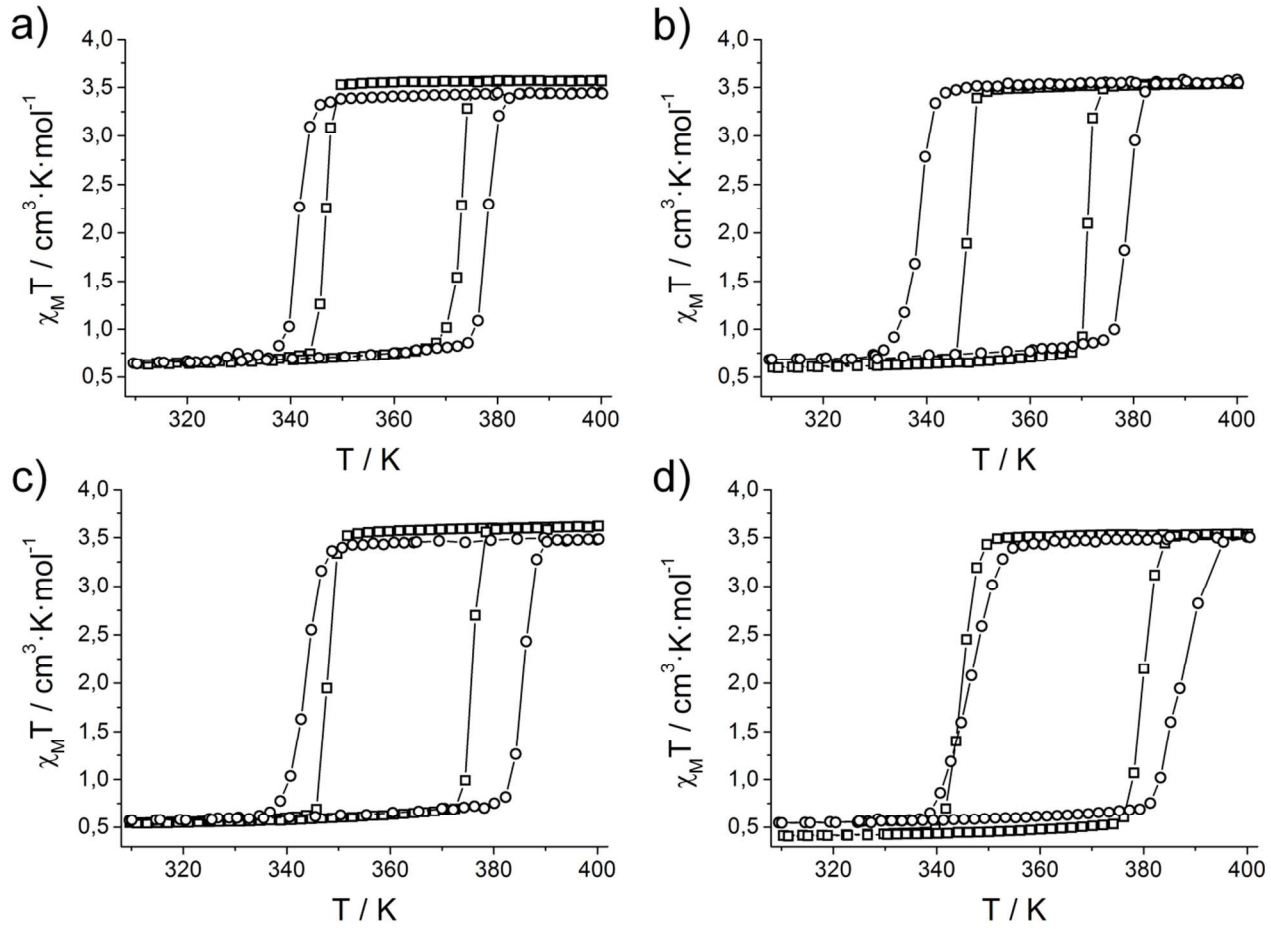

Fig. 4 Comparison of the thermal variation of the $\chi_M T$ product for the Fe-Trz (□) and Fe-Trz@SiO_2 (○) nanoparticles studied in this work: a) **1** and **1@SiO$_2$**; b) **2** and **2@SiO$_2$**; c) **3** and **3@SiO$_2$**; d) **4** and **4@SiO$_2$**.

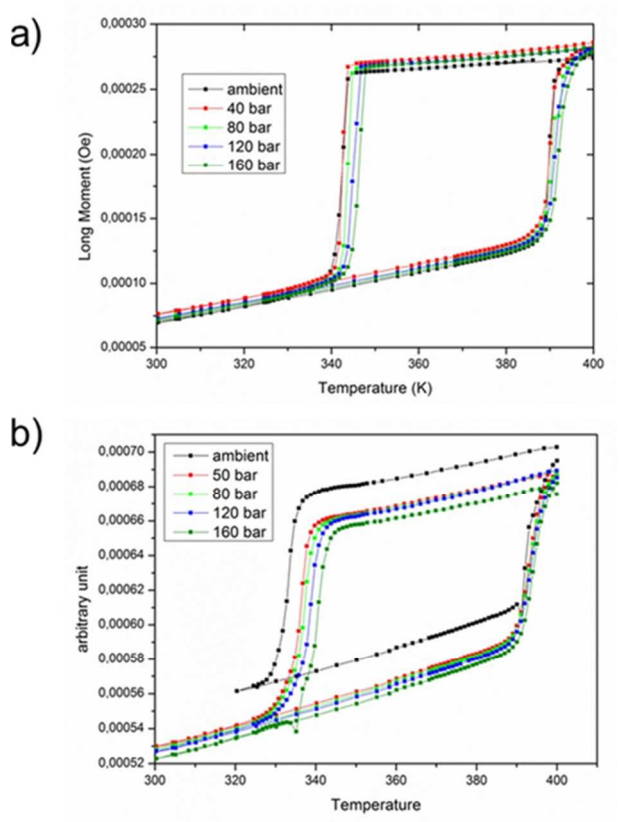

Fig. 5 Temperature dependence of $\chi_M T$ under hydrostatic pressure for **4** (a) and **4@SiO₂** (b).

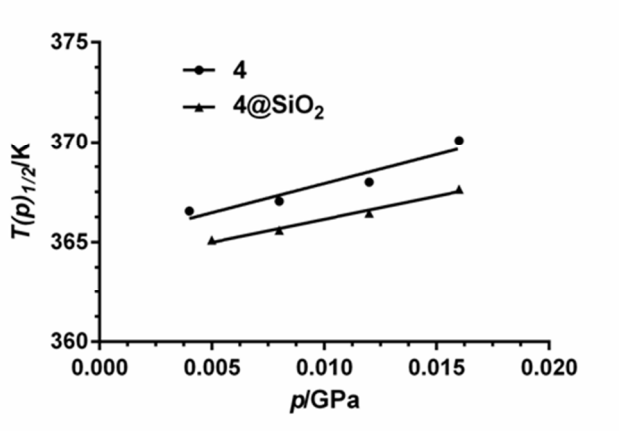

Fig. 6 Pressure dependence of T_C for **4** and **4@SiO₂**.

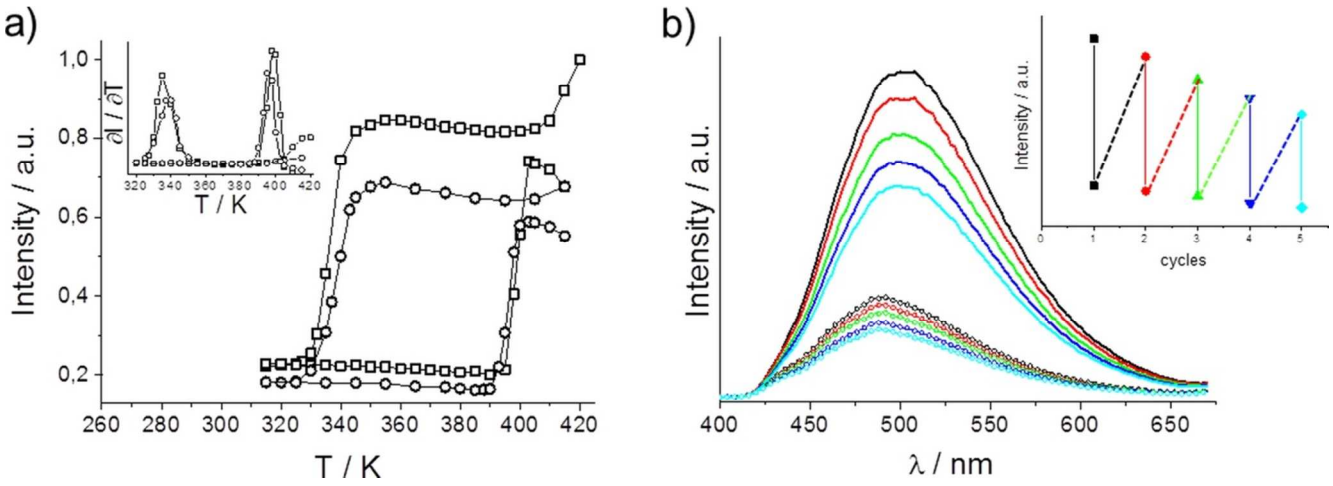

Fig. 7 a) Thermal variation of the emission intensity at λ_{exc} = 495 nm for sample **1-dansyl** (open squares: cycle 1; open circles: cycle 2). b) Variation of the emission intensity for sample **1-dansyl** after successive heating (400 K, full lines) and cooling (300 K, dotted lines) cycles. The gradual and irreversible decrease of emission intensity after each cycle confirms the thermal decomposition of the dansyl groups at 400 K.

Cite this: DOI: 10.1039/c0xx00000x

www.rsc.org/xxxxxx

ARTICLE TYPE

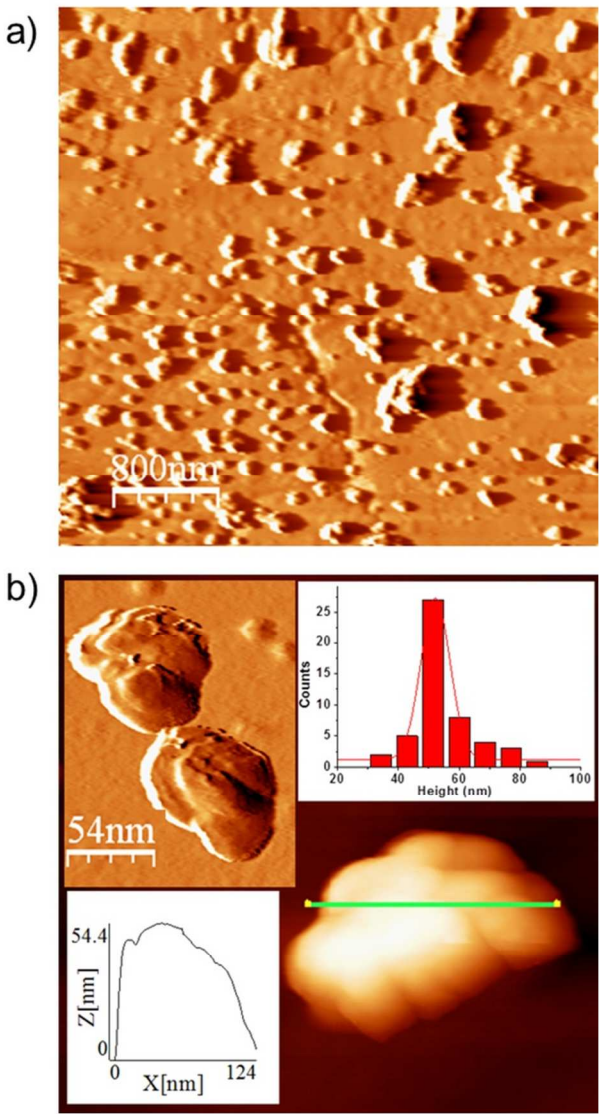

Fig. 8 a) AFM image of an homogeneous distribution of **1@SiO$_2$-SH** nanoparticles deposited on a gold surface. The inset represents the size distribution of the nanoparticles. The data of the histogram were collected from 50 randomly picked particles. b) AFM zoomed image of a representative particle found with a height profile (the inset).

Table 1 Average particle size for samples described in this work.[a]

	Length (nm)	Width (nm)
1	28.3 ± 2.9	-----
2	38.4 ± 2.6	----
3	70.3 ± 6.5	59.0 ± 4.3
4	321.2 ±17.1	194.9 ± 16.3
1@SiO$_2$	55.7 ± 3.9	----
2@SiO$_2$	87.4 ± 7.5	67.9 ± 9.2
3@SiO$_2$	147.7 ± 11.7	92.1 ± 12.1
4@SiO$_2$	422.4 ± 50.3	179.8 ± 42.1

[a] At least 50 nanoparticles for each sample were evaluated to determine the average dimensions of the particles.

Table 2 Physical parameters characteristic for the thermal induced spin transition of the materials studied in this work.

	$T_c\downarrow$ (K)[a]	$T_c\uparrow$ (K)[a]	ΔT_c	% HS_{320K}[b]
1	347	373	26	17.6
2	347	371	24	17.0
3	348	376	28	15.1
4	345	380	35	11.7
1@SiO$_2$	341	378	37	19.2
2@SiO$_2$	339	379	40	19.2
3@SiO$_2$	343	385	42	16.3
4@SiO$_2$	346	387	41	15.6

[a] $T_c\downarrow$ and $T_c\uparrow$ are the critical temperatures for the HS → LS and LS → HS transitions in the cooling and warming mode respectively. [b] Percentage of residual Fe(II) ions that remain in the HS state below $T_c\downarrow$.

Notes and references

[a] *Departamento de Química Inorgánica, Facultad de Ciencias, Universidad de Granada. Avda. Fuentenueva s/n, 18071, Granada, Spain. Fax: +34 958248526; Tel: +34 958 248094. Email: jmherrera@ugr.es, ecolacio@ugr.es.*
[b] *School of Chemistry, Main Building, Cardiff University, Cardiff CF10 3AT, UK. Fax: +44 2920874030; Tel: +44 2920879316.*
[c] *Departamento de Química Inorgánica, Universidad Autónoma de Madrid, 28049 Madrid, Spain. E-mail: felix.zamora@uam.es*
[d] *Departamento de Ciencia de los Materiales e Ingeniería Metalúrgica y Química Inorgánica, Facultad de Ciencias, Universidad de Cádiz, 11510, Puerto Real, Cádiz, Spain.*
[e] *Centre for Science at Extreme Conditions, The University of Edinburgh, Erskine Williamson Building, Peter Guthrie Tait Road, the King's Buildings, Edinburgh, EH9 3FD, United Kingdom.*
[f] *EaStCHEM School of Chemistry, The University of Edinburgh, West Mains Road, Edinburgh, EH9 3JJ, United Kingdom.*

† Electronic Supplementary Information (ESI) available: [HRTEM and HRSEM images of the bulk FeHTrz polymer. Elemental analysis of the samples described in this work. Thermal variation of the $\chi_M T$ product for **1-dansyl** and HRTEM image of the nanoparticles.AFM images of **1@SiO$_2$-SH** nanoparticles deposited on a gold surface at different immersion times. Movie of the tomographic reconstruction of sample **3@SiO$_2$**]. See DOI: 10.1039/b000000x/

‡ Footnotes should appear here. These might include comments relevant to but not central to the matter under discussion, limited experimental and spectral data, and crystallographic data.

1 a) P. Gütlich, H. A. Goodwin (Eds.), *Spin Crossover in Transition Metal Compounds.* Topics in Current Chemistry **2004**, 233-235; b) M. A. Halcrow (Ed.), *Spin-crossover materials, properties and applications.* Willey (UK), **2013**.)
2 see for example: a) J. A. Real, A. B. Gaspar, V. Niel, M. C. Muñoz, *Coord. Chem. Rev.* **2003**, *236*, 121-141; b) P. Gütlich, A. Hauser, H. Spiering, *Angew. Chem. Int. Ed.* **1994**, *33*, 2024-2054. c) A. B. Gaspar, V. Ksenofontov, M. Seredyuk, P. Gütlich, *Coord. Chem. Rev.* **2005**, *249*, 2661-2676; d) A. Galet, A. B. Gaspar, M. C. Muñoz, G. V. Bukin, G. Levchenko, J. A. Real, *Adv. Mater.* **2005**, *17*, 2949-2953; e) N. Ould-Mousa, G. Mólnar, S. Bonhommeau, A. Zwick, S. Mouri, K. Tanaka, J. A. Real, A. Bousseksou, *Phys. Rev. Lett.,* **2005**, *94*, 107205,1-4; f) M. Ohba, K. Yoneda, G. Agustí, M. C. Muñoz, A. B. Gaspar, J. A. Real, M. Yamasaki, H. Ando, Y. Nakao, S. Sakaki, S. Kitagawa, *Angew. Chem. Int. Ed.,* **2009**, *48*, 4767-4771; g) S. M. Neville, G. J. Halder, K. W. Chapman, M. B. Duriska, P.D. Southon, J. D. Cashion, J. F. Létard, B. Moubaraki, K. S. Murray, C. J. Kepert, *J. Am. Chem. Soc.,* **2008**, *130*, 2869-2876.)
3 a) O. Kahn, C. Jay Martinez, *Science*, **1998**, *279*, 44-48; b) O. Kahn, J. P. Launay, *Chemtronics*, **1988**, *3*, 140.
4 a) A. Bousseksou, G. Molnár, L. Salmon, W. Nicolazzi, *Chem. Soc. Rev.* **2011**, *40*, 3313; b) H. J. Shepherd, G. Molnár, W. Nicolazzi, L. Salmon, A. Bousseksou, *Eur. J. Inorg. Chem.*, **2013**, 653; c) G. Molnár, L. Salmon, W. Nicolazzi, F. Terki, A. Bousseksou, *J. Mater. Chem. C*, **2014**, *2*, DOI: 10.1039/c3tc31750a)
5 a) O. Roubeau, *Chem. Eur. J.*, **2012**, *18*, 15230; b) M. C. Muñoz, J. A. Real, *Coord. Chem. Rev.*, **2011**, *255*, 2068
6 a) I. Boldog, Ana B. Gaspar, V. Martínez, P. Pardo-Ibánez, V. Ksenofontov, A. Bhattacharjee, P. Gütlich, J. A. Real, *Angew. Chem. Int. Ed.* **2008**, *47*, 6433-6437; b) F. Volatron, L. Catala, E. Rivière, A. Gloter, O. Stéphan, T. Mallah, *Inorg. Chem.* **2008**, *47*, 6584-6586)
7 a) T. Forestier, S. Mornet, N. Daro, T. Nishihara, S. Mouri, K. Tanaka, O. Fouché, E. Freysz, J. F. Létard, *Chem. Commun.,* **2008**, 4327-4329; b) T. Forestier, A. Kaiba, S. Pechev, D. Denux, P. Guionneau, C. Etrillard, N. Daro, E. Freysz, J. F. Létard, *Chem. Eur. J.,* **2009**, *15*, 6122-6130.
8 a) E. Coronado, J. R. Galán-Mascarós, M. Monrabal-Capilla, J. García-Martínez, P. Pardo-Ibánez, *Adv. Mater.,* **2007**, *19*, 1359-1361; J. R. Galán-Mascarós, E. Coronado, A. Forment-Aliaga, M. Monrabal-Capilla, E. Pinilla-Cienfuegos, M. Ceolin, *Inorg. Chem.,* **2010**, *49*, 5706-5714.
9 Y. Raza, F. Volatron, S. Moldovan, O. Ersen, V. Huc, C. Martini, F. Brisset, A. Gloter, O. Stéphan, A. Bousseksou, L. Catala, T. Mallah, *Chem. Commun.,* **2011**, *47*, 11501-11503.
10 P. Durand, S. Pillet, E. Bendeif, C. Carteret, M. Bouazaoui, H. E. Hamzaoui, B. Capoen, L. Salmon, S. Hérbert, J. Ghanbaja, L. Aranda, D. Schaniel, *J. Mater. Chem. C,* **2013**, *1*, 1933.
11 S. Titos-Padilla, J. M. Herrera, X. –W. Chen, J. J. Delgado, E. Colacio, *Angew. Chem. Int. Ed.,* **2011**, *50*, 3290-3293.
12 H. J. Shepherd, C. M. Quintero, G. Molnár, L. Salmon, A. Bousseksou, *Luminescent Spin-Crossover Materials (pp. 347 - 373), Spin-Crossover Materials, properties and applications, Ed. Malcom A. Halcrow, Wiley, **2013**.*
13 L. Salmon, G. Molnár, D. Zitouni, C. Quintero, C. Bergaud, J. –C. Micheau, A. Bousseksou, *J. Mater. Chem.*, **2010**, *20*, 5499-5503.
14 C. M. Quintero, I. A. Gural'skiy, L. Salmonm G. Molnar, C. Bergaud, A. Bousseksou, *J. Mater. Chem.*, **2012**, *22*, 3745-3751.
15 J. Kröber, J. Audière, R. Claude, E. Codjovi, O. Kahn, *Chem. Mater.,* **1994**, *6*, 1404.
16 K. V. Kamenev, S. Tancharakorn, N. Robertson, A. Harrison, *Rev. Scientific Instruments,* **2006**, *77*, 07395.
17 a) E. Coronado, J. R. Galán-Mascarós, M. Monrabal-Capilla, J. García-Martínez, P. Pardo-Ibánez, *Adv. Mater.* **2007**, *19*, 1359-1361; b) F. Volatron, L. Catala, E. Rivière, A. Gloter, O. Stéphan, T. Mallah, *Inorg. Chem.* **2008**, *47*, 6584-6586.
18 a) G. Félix, W. Nicolazzi, L. Salmon, G. Molnar, M. Perrier, G. Maurin, J. Larionova, J. Long, Y. Guari, A. Bousseksou, *Phys. Rev. Lett.* **2013**, *110*, 235701; b) V. Martínez, I. Boldog, A. B. Gaspar, V. Ksenofontov, A. Bhattacharjee, P. Gütlich, J. A. Real, *Chem. Mater.*

2010, *22*, 4271-4281; c) A. Tissot, L. Rechignat, A. Bousseksou, M. L. Boillot, *J. Mater. Chem.* **2012**, *22*, 3411-3419.
19 P. Gütlich, V. Ksenofontov, A. B. Gaspar, *Coord. Chem. Rev.* **2005**, *249*, 1811–1829., Vadim Ksenofontov, Ana B. Gaspar, Philipp Gütlich, Top. Curr. Chem. 2004, 235, 23-64.
20 a) E. Meissner, H. Köppen, H. Spiering, P. Gütlich, *Chem. Phys.Lett.* **1983**, *95*, 163–166. H. Spiering, E. Meissner, H. Köppen, E. W. Müller, P. Gütlich *Chem. Phys.* **1982**, *68*, 65–71; b) P. Adler, L. Wiehl, E. Meissner, C. P. Köhler, H. Spiering, P.Gütlich, *J. Phys. Chem. Solids* **1987**, *48*, 517–525.
21 Y. García, P. J. van Koningsbruggen, R. Lapouyade, L. Fournés, L. Rabardel, O. Kahn, V. Ksenofontov, G. Levchenko, P. Gutlich, *Chem. Mater.* **1998**, *10*, 2426
22 A. B. Gaspar, G. Agustí, V. Martínez, M. C. Muñoz, G. Levchenko, J. A. Real, *Inorg. Chim. Acta*, **2005**, *358*, 4089-4094.
23 A. B. Gaspar, M. C. Muñoz, N. Moliner, V. Ksenofontov, G. Levchenko, P. Gütlich, J. A. Real, *Monatsh. Chem*., **2003**, *134*, 285-294.
24 a) C. P. Köhler, R. Jakobi, E. Meissner, L. Wiehl, H. Spiering, P. Gütlich, *J. Phys. Chem. Solids*, **1990**, *51*, 239; b) T. Kohlhaas, H. Spiering, P. Gütlich, *Z. Physik B*, **1997**, *102*, 455; c) H. Romstedt, A. Hauser, H. Spiering, *J. Phys. Chem. Solids*, **1998,** *59*, 265)
25 V. Balzani, G. Bergamini, S. Campagna, F. Puntoriero, *Top. Curr. Chem.* **2007**, *280*, 1-36.
26 J. R. Lakowicz, *Principles of Fluorescence Spectroscopy, 3rd Ed.*,**2006**, Springer.
27 S. Titos-Padilla, E. Colacio, S. J. A. Pope, J. J. Delgado, M. Melgosa, J. M. Herrera, *J. Mater. Chem. C*, **2013**, *1*, 3808.

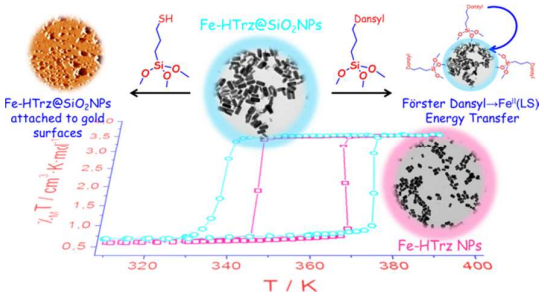

The surface of SiO_2-coated Fe-Triazole SCO nanoparticles has been functionalized with dansyl luminophores. When thiol groups are grafted, the nanoparticles can be deposited onto gold surfaces.